

# Evidence of sharp transitions between octahedral and capped trigonal prism states of the solvation shell of $\text{Fe}^{+3}(\text{aq})$

Amrita Goswami,<sup>†</sup> Alejandro Peña-Torres,<sup>†</sup> Elvar Ö. Jónsson,<sup>†</sup> Sergei A. Egorov,<sup>†,‡</sup> and Hannes Jónsson<sup>\*,†</sup>

<sup>†</sup>*Science Institute and Faculty of Physical Sciences, University of Iceland, VR-III, 107 Reykjavík, Iceland*

<sup>‡</sup>*Department of Chemistry, University of Virginia, Charlottesville, Virginia 22901, USA*

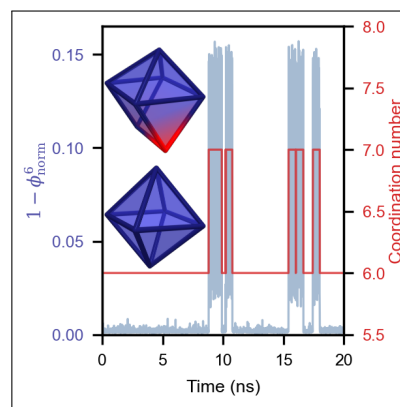
E-mail: hj@hi.is

## Abstract

A discrepancy has been reported in the literature between experimental measurements and density functional theory (DFT) calculations, on the one hand, and simulations based on empirical potential energy functions on the other hand, regarding the solvation shell of the aqueous  $\text{Fe}^{3+}$  ion; the former studies reporting a coordination number of 6.0 corresponding to a well defined octahedral solvation shell, while the latter studies report a higher value, typically around 6.5. The simulations presented here were conducted for long time intervals and a wide range in ion concentration, using various potential energy functions as well as DFT calculations for several of the generated configurations. The results indicate that the solvation shell can undergo abrupt transitions between two well-separated states: an octahedral state (OH) with 6-fold coordination and a high degree of sphericity,  $\phi^6$ , and a capped trigonal prism (CTP) state with 7-fold coordination and significantly smaller  $\phi^6$ . In dilute  $\text{FeCl}_3$  solutions, with ion concentration on the order of  $0.1 \text{ mol/dm}^3$  ( $[\text{Fe}^{3+}]/[\text{H}_2\text{O}]$  ratio of 1:600), the lifetime of the two states is similar, on the order of a ns, but the lifetime of the OH state increases with ion concentration, while that of the CTP state remains roughly constant. When

a uniform negative background is used instead of explicit counterions, as is often done in DFT calculations, the lifetime of the OH state increases strongly, quadrupling as the ion concentration is increased to  $0.9 \text{ mol/dm}^3$ . Experimental measurements of lower concentration solutions, as well as corresponding simulations based on electronic structure calculations spanning at least several nanoseconds, are needed to test the existence of the predicted CTP state.

## TOC Graphic



One of the fundamental tasks in physical chemistry is to gain an understanding of ion solvation, especially in water solutions. A key issue is the solvent shell that forms around the ions, which can dictate their chemical and physical properties.<sup>1</sup> Experimental measurements of solvation shells are challenging, and computer simulations can provide complementary microscopic insight into their structure and dynamics. Over the past two decades, several potential energy functions have been developed to model ion-water interactions.<sup>2-7</sup> Simulations based on recently developed functions for describing the interaction between ions and rigid point charge water models have been able to successfully reproduce both the experimentally measured solvation free energy and the ion-oxygen distance for a wide range of aqueous ionic solutions.<sup>8-13</sup> While solvation shells of aqueous transition metal ions typically correspond to sixfold coordination in an octahedral structure, sevenfold coordination shells have, in some rare cases, also been reported.<sup>14-18</sup> For example, both theoretical and experimental evidence has been presented for the existence of a flexible hepta-coordinated Hg (II) aqua ion.<sup>19</sup>

A particularly relevant system is the solvation of Fe(III) ions in water, for which the prevailing view of the solvation shell is a well-defined octahedral arrangement of six H<sub>2</sub>O molecules.<sup>20</sup> While simulations using empirical potential functions for this system have also been successful in reproducing various properties such as the average Fe-O distance and solvation free energy, the predicted coordination number of Fe(III) has turned out to be significantly greater than 6.0, in the range of 6.3 to 6.9. This departure from the conventionally expected coordination number has been dismissed as an artefact of potential functions based on point charges, and the 12-6 or 12-6-4 functional form.<sup>8,9,12</sup>

As a result, there have been various attempts to explicitly restrain the coordination number to 6.0. For instance, the atomic charges on the six neighbouring water molecules have been modified to obtain a hexa-coordinated solvation shell, but this has the unfortunate side effect of eliminating the possibility of ligand exchange.<sup>21</sup>

Alternatively, the positive charge of the Fe(III) ion has been distributed on six sites near the central metal ion in the desired predefined octahedral coordination geometry.<sup>22,23</sup> This class of models allows for the possibility of ligand exchange but has the drawback that different types of solvation shells, such as the experimentally observed tetrahedral [FeCl<sub>4</sub>]<sup>-</sup> ion, cannot be reproduced.<sup>24-27</sup>

Experimental measurements on ferric chloride solutions have led to a plethora of reported solvation structures, including the tetrahedral [FeCl<sub>4</sub>]<sup>-</sup>, octahedral *trans*-[FeCl<sub>2</sub>(H<sub>2</sub>O)<sub>4</sub>]<sup>+</sup>, [FeCl<sub>3</sub>(H<sub>2</sub>O)<sub>3</sub>], and [FeCl(H<sub>2</sub>O)<sub>5</sub>]<sup>2+</sup>.<sup>24-34</sup> The experimental results indicate that the solvation shell structure is strongly dependent on ion concentration,<sup>35-37</sup> and a point of some contention is the identity of the dominant Fe<sup>3+</sup> form in concentrated ferric chloride solutions, with ion concentration on the order of 1 mol/dm<sup>3</sup>. A recent EXAFS (Extended X-Ray Absorption Fine Structure) concludes that the prevailing species is *trans*-[FeCl<sub>2</sub>(H<sub>2</sub>O)<sub>4</sub>]<sup>+</sup> at this high concentration, while for a low concentration of 0.001 mol/dm<sup>3</sup> the measurements are found to be consistent with [Fe(H<sub>2</sub>O)<sub>6</sub>]<sup>3+</sup>.<sup>35</sup> X-ray and neutron diffraction experiments on dilute solutions can be impeded by low signal intensity, however, EXAFS is considered to be a suitable technique to examine the structure of dilute aqueous ionic solutions.<sup>38</sup> While results from Persson<sup>35</sup> and other measurements of low concentration solutions<sup>1,39</sup> point to the conclusion that the solvation shell consists only of H<sub>2</sub>O, it is not entirely clear whether the coordination number is precisely 6.0.<sup>1</sup>

Unlike the calculations based on potential energy functions, the simulations where energy and atomic forces are obtained from density functional theory (DFT), using either the PBE<sup>40,41</sup> or B3LYP<sup>42-44</sup> functional approximations, have not shown deviations from the octahedral form of the solvation shell and are found to be consistent with a coordination number of 6.0.<sup>40-44</sup> As the computational effort is large, the time interval represented by such simulations has necessarily been short, spanning at most a few tens of ps, and an indication of a change in the structure of the first solvation

shell has not been found.<sup>41,44</sup> The simulations have, furthermore, been carried out using a uniform negative background charge instead of explicit counterions and for a high  $\text{Fe}^{3+}$  concentration corresponding to a  $[\text{Fe}^{3+}]/[\text{H}_2\text{O}]$  ratio ranging from 1:18 to 1:137. These are much higher ion concentrations than have been used in the simulations based on potential energy functions, 1:600<sup>9</sup> to 1:1085.<sup>8,12</sup>

In the present study, we address the disparity between DFT calculations and simulations with potential energy functions, cognizant of differences in ion concentration and simulation conditions. We systematically investigate the structure of the solvation shell of  $\text{Fe}^{3+}$  ions in water using a sphericity measure and perform extensive simulations with several potential functions, over a wide range of ion concentrations, with explicit counterions as well as uniform negative background, and for long time intervals. The results show remarkably clear and abrupt changes between two states of the solvation shell, an octahedral state corresponding to sixfold coordination and a capped trigonal prism (CTP) state with 7-fold coordination. The effects of ion concentration and the presence of explicit counterions versus uniform background charge on the solvation structure are found to be strong and can help reconcile the reported controversy between the different types of simulation approaches. Results of DFT calculations are also presented for selected molecular configurations obtained from the simulations providing structures corresponding to a CTP state obtained after local energy minimization.

In addition to the coordination number, the structure of the solvation shell is characterized using the sphericity of the convex hull. In this way, we devise a new and robust order parameter for distinguishing between octahedral and non-octahedral structures. Sphericity is a measure of how similar a 3-dimensional shape is to a perfect sphere. It is defined as the ratio of the surface area of a sphere with the same volume as the shape considered, to the actual surface area of the shape:<sup>45</sup>

$$\phi = \frac{\pi^{\frac{1}{3}}(6V_s)^{\frac{2}{3}}}{A_s}, \quad (1)$$

where  $V_s$  and  $A_s$  are the volume and surface area of the shape, respectively.

Originally formulated for analyzing sedimentary rock fragments,<sup>45</sup> the sphericity has been used in diverse applications, including nanoparticle synthesis,<sup>46–48</sup> nanofluid thermal conductivity,<sup>49,50</sup> nanoparticle aggregation in fluidized beds,<sup>51</sup> hypersensitivity reactions to liposomal drugs,<sup>52,53</sup> cancer research,<sup>54–58</sup> and nanomedicine.<sup>59</sup>

We define  $\phi^6$  as the sphericity of the convex hull formed by the closest six neighbouring oxygen atoms of the Fe ion center. The sphericity of a perfect octahedron is 0.846<sup>60–62</sup> and we divide by this number to define a normalized sphericity,  $\phi_{\text{norm}}^6$ , which then can have a maximum value of 1.0.

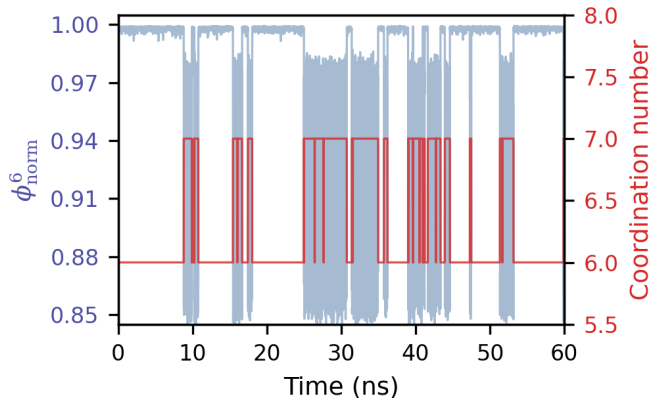


Figure 1: Time evolution of the coordination number (red) and the normalized sphericity (blue),  $\phi_{\text{norm}}^6$ , of the convex hull formed by the first six neighbours of the Fe ion in a room temperature simulation of a  $\text{FeCl}_3$  solution with concentration corresponding to a  $[\text{Fe}^{3+}]/[\text{H}_2\text{O}]$  ratio of 1:597, using the *a99SB-disp* potential function.<sup>9</sup> Both measures of the solvation shell structure show abrupt transitions between sustained states corresponding to octahedral and capped trigonal prism configurations. The average coordination turns out to be 6.4 in this case.

The normalized sphericity,  $\phi_{\text{norm}}^6$ , turns out to be a robust metric for distinguishing between octahedral (OH) and non-octahedral solvation

shell structures. Figure 1 shows a comparison between  $\phi_{\text{norm}}^6$  and the coordination number, characterizing the time evolution of the solvation shell in a system with a  $[\text{Fe}^{3+}]/[\text{H}_2\text{O}]$  ratio of 1:597. The normalized sphericity,  $\phi_{\text{norm}}^6$ , mirrors trends in the coordination number, and is, moreover, less sensitive to instantaneous thermal deformations. Unless explicitly stated, the simulations are carried out using the 12-6 Fe-H<sub>2</sub>O parametrization with the a99SB-*disp* water model,<sup>9</sup> with chloride counterions (see Methods section). The coordination number is calculated as the number of neighbours within a cutoff distance of 2.60 Å, a value selected based on the results shown in Figure 2.

Figure 2(a) depicts a scatter plot of  $\phi_{\text{norm}}^6$  and the distance to the seventh closest water molecule from the Fe<sup>3+</sup> ion,  $r_7$ . Clusters were obtained using DBSCAN (density-based spatial clustering of applications with noise),<sup>63–65</sup> a clustering algorithm that groups data points based on their density, thereby identifying clusters of high-density regions and classifying outliers as noise. Octahedral and non-octahedral configurations form two distinct clusters, which can be differentiated simply by using a single  $\phi_{\text{norm}}^6$  criterion, as shown by the horizontal dashed black line in Figure 2(a). The non-octahedral configurations correspond to a 7-fold coordination, with the water molecules at the vertices of an augmented triangular prism. This is also referred to as the CTP geometry, with  $C_{2v}$  symmetry.<sup>66,67</sup> Such a structure has been observed for transition metal complexes.<sup>14–18</sup> Our analysis shows two types of CTP configurations, which we refer to as ‘prism acquisition’ and ‘pyramid acquisition’ structures. They have the same shape and geometry but differ in the position of the seventh H<sub>2</sub>O molecule. We did not observe structures where the seventh molecule resides at any of the pyramid base vertices.

Figure 2(b)-(c) depicts an idealized augmented triangular prism with all seven vertices equidistant from the center. The position of the extra water molecule highlighted is in red. The convex hull formed by the closest six neighbours in the prism acquisition structure (Figure 2(b)) tends to be less flattened, compared

to that formed by the the pyramid acquisition structure (Figure 2(c)). Moreover, the convex hull resembles that of a distorted octahedron in the case of the prism acquisition structure. A mechanism for the formation of the extended solvation shell is indicated, wherein the seventh closest water molecule tends to capture one of the prism apex vertices during its approach. A prism acquisition structure can subsequently deform or evolve into a pyramid acquisition structure. Furthermore, as the seventh furthest water molecule is ejected from the first solvation shell, it occupies a prism apex vertex.

With the help of this  $\phi_{\text{norm}}^6$  criterion, we can differentiate between OH and CTP configurations and evaluate the lifetime of each state. We posit that solvation structural properties and behaviour arise directly from two separate contributions: those from the OH state, and from the CTP state.

We define the average lifetime,  $\tau$ , of a particular state as  $\tau = \frac{1}{N} \sum_{i=1}^N t_i^{\text{end}} - t_i^{\text{begin}}$ , for every interval  $i \in [1, N] \subset \mathcal{N}$  in which the current configuration persists without switching to the other state, where  $t$  represents the elapsed simulation time. This metric embodies the switching frequency between states, and is an indication of the stability of a particular state. On the other hand, the propensity of the system to exist in a particular configuration can be described by the probability,  $p$ , of observing that state, *i.e.* the ratio of the total time spent in the state, to the total simulation time. Both of these metrics directly influence other average structural measures, such as the coordination number (CN), the average distance of the first six neighbours from the Fe ion center ( $\overline{r_{i \leq 6}}$ ), ion-oxygen distance (IOD), etc. In the previous literature, the CN and IOD have been reported for various potential energy functions;<sup>8,9,12</sup> however, the simulation time has typically been short, on the order of 10 ns, which may not capture the long-term structural dynamics and proper averaging over the OH and CTP states. Consequently, long simulations on the order of 100 ns, are carried out here for a range in ion concentration in order to characterize the structure of the solvation shell.

Our classical dynamics simulations show that

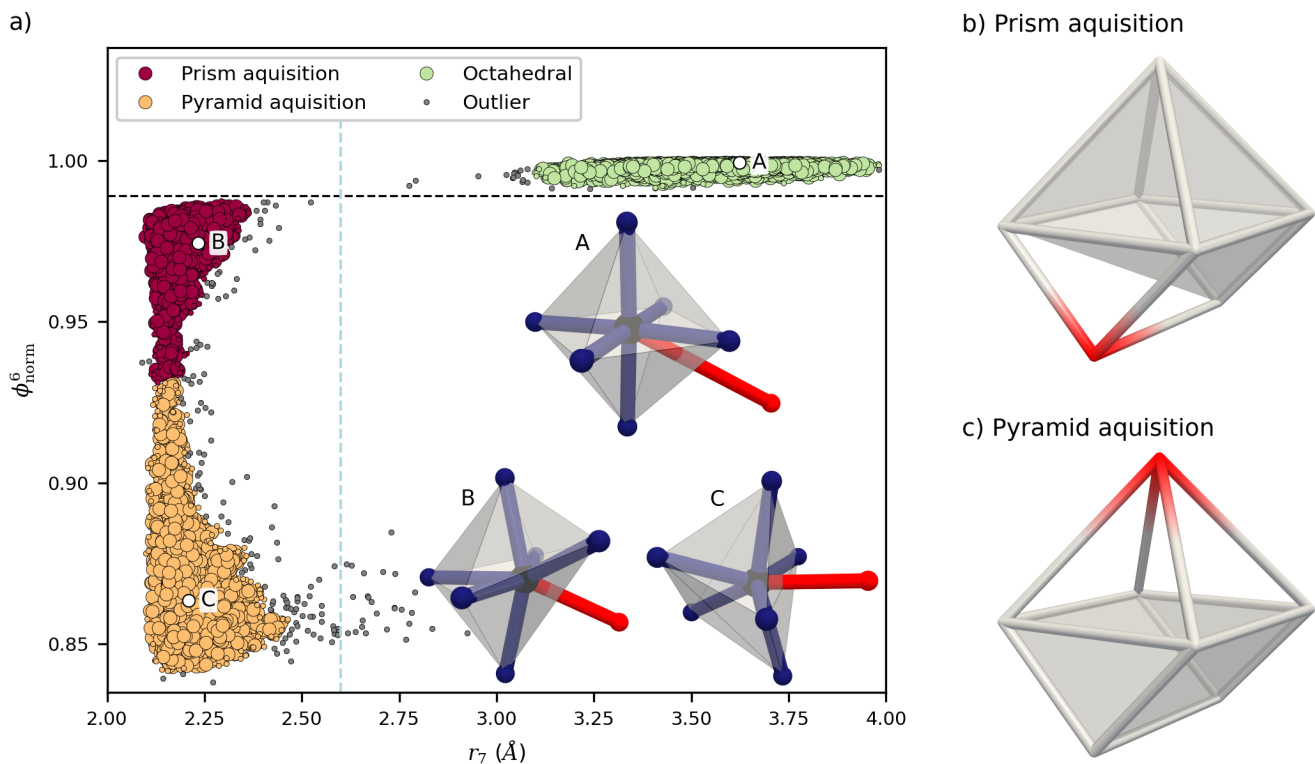


Figure 2: (a) The normalized sphericity,  $\phi_{\text{norm}}^6$ , as a function of the distance to the seventh water molecule from the Fe ion,  $r_7$ . Each point is coloured according to its inclusion in a particular cluster, corresponding to its structural type. Outliers are depicted as small grey circles. The size of a point belonging to a particular cluster indicates whether it is a core point (large circle) or a non-core point that forms an edge of the cluster (small circle). Insets depict the Fe ion (black) and surrounding oxygen atoms (hydrogen atoms are omitted for clarity), with the convex hull of the first six neighbours shown in translucent grey, for A) an octahedral configuration, B) a prism acquisition structure and C) a pyramid acquisition configuration. The first six neighbouring O atoms and the seventh closest atom are blue and red, respectively. Octahedral and non-octahedral configurations can be classified using a single  $\phi_{\text{norm}}^6$  criterion, as shown by the black dashed line separating the two clusters. The light-blue dashed line shows the value of the cutoff used in calculations of the coordination number. The data were obtained from a 150 ns trajectory for a  $[\text{Fe}^{3+}]/[\text{H}_2\text{O}]$  ratio of 1:597. (b) An idealized augmented triangular prism with vertices equidistant from the center. One of the prism apex vertex positions is coloured in red, depicting where the seventh molecule would be located if this were a prism acquisition structure. The other six vertices and the convex hull formed by them are grey. (c) An analogous pyramid acquisition structure.

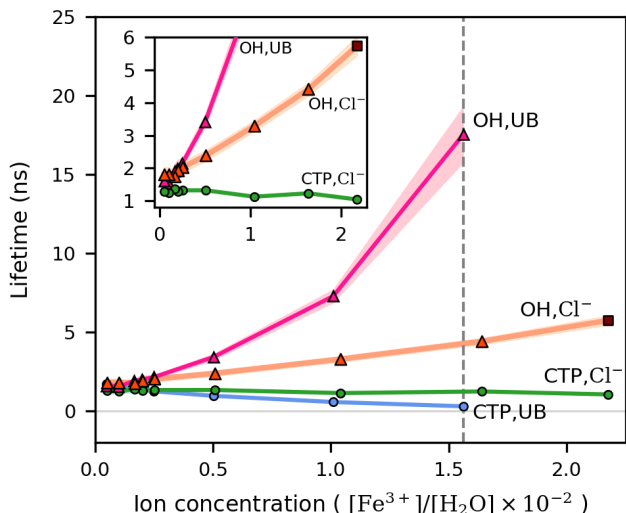


Figure 3: Calculated lifetime,  $\tau$ , of the OH state and the CTP state as a function of the ion concentration, for systems with explicit counterions ( $\text{Cl}^-$ ) and systems with uniform negative background charge (UB). Data from simulations performed with explicit counterions are denoted by orange-red markers for the OH state and sea-green circles for the CTP state. The OH configurations all correspond to  $[\text{Fe}(\text{H}_2\text{O})_6]^{3+}$ , except for the brown marker representing a concentration at which a small proportion of the *trans*- $[\text{FeCl}_2(\text{H}_2\text{O})_4]^+$  was observed along with the predominant  $[\text{Fe}(\text{H}_2\text{O})_6]^{3+}$ . The lifetime of the OH state increases with ion concentration, while the lifetime of the CTP state is quite insensitive to concentration. Therefore, the relative probability of the OH state increases with increasing ion concentration. Results of simulations using uniform background charge are shown by pink triangles for OH and blue circles for CTP. The dashed grey line shows the concentration used in the DFT calculations. The uniform background charge gives results that are significantly different from those with explicit counterions when the ion concentrations is greater than a ratio of about 1:400. An inset shows a close-up view, depicting how the OH lifetime with counterions and uniform background charge increase with ion concentration. A light grey solid line represents zero lifetime.

the ion concentration can have strong effect on the solvation shell. Figure 3 depicts changes in the average lifetime of the OH and CTP states as the ion concentration is varied for systems with explicit counterions (orange and sea-green markers, respectively). The increase in the lifetime of the OH state,  $\tau_{\text{OH}}$ , is large enough that the value of  $\tau_{\text{OH}}$  at a concentration that is typical for simulations based on potential energy functions ( $[\text{Fe}^{3+}]/[\text{H}_2\text{O}]$  ratio of 1:597)<sup>9,11</sup> is about 1.75 ns, while at a concentration of ( $[\text{Fe}^{3+}]/[\text{H}_2\text{O}]$  of 1:61), roughly equivalent to that used in previous DFT based calculations,<sup>44</sup> it is 2.5 times longer. The average lifetime of the CTP state, however,  $\tau_{\text{CTP}}$ , turns out to be relatively insensitive to the ion concentration. This implies that, for a high ion concentration (or for a small periodic simulation box size), the probability of observing the CTP state,  $p_{\text{CTP}}$ , is low.

DFT calculations, furthermore, tend to employ a uniform background charge, in lieu of explicit counterions. Figure 3 shows a comparison of trends in  $\tau_{\text{OH}}$  and  $\tau_{\text{CTP}}$ , for systems with a uniform background charge and those with explicit counterions. For low concentration, less than 1:400, the results with uniform background charge agree, within error bars, with data from simulations with explicit counterions. There is, however, significant difference between the two for a concentration typical of DFT calculations, depicted by a dashed grey line ( $[\text{Fe}^{3+}]/[\text{H}_2\text{O}]$  of 1:64). We also note that, at the higher ion concentration, the value of  $\tau_{\text{CTP}}$ , with uniform background charge (blue circles), also concomitantly decreases, thereby further reducing the probability of observing the CTP state under such conditions. These results show that the uniform background charge tends to spuriously favour the OH state and destabilize the CTP state. These results indicate that in order to test whether the CTP state is present at the DFT level of theory, it would be necessary to carry out simulations with significantly lower ion concentration, including explicit counterions instead of uniform background, and over a time interval that is significantly longer than a ns.

We also note that for the highest con-

centration considered here, with counterions, (filled brown square) a small proportion of the *trans*-  $[\text{Fe}(\text{H}_2\text{O})_4\text{Cl}_2]^+$  is formed, in addition to the dominant octahedral  $[\text{Fe}(\text{H}_2\text{O})_6]^{3+}$  configuration, and low quantities of the CTP state,  $[\text{Fe}(\text{H}_2\text{O})_7]^{3+}$ . Interestingly, this *trans*-  $[\text{Fe}(\text{H}_2\text{O})_4\text{Cl}_2]^+$  structure is an experimentally observed species at high concentration on the order of 1 mol/dm<sup>3</sup>.<sup>35</sup> This implies that the potential energy function employed here can, at least qualitatively, approximate some features of the rich structural behaviour exhibited by concentrated ferric chloride solutions.

To further assess the stability of the CTP state, we optimized a set of eight systems comprising 64 water molecules and a  $\text{Fe}^{3+}$  ion using DFT with the PBE functional approximation. A simulation was first carried out for a concentration of 1:600 using the a99SB-*disp* potential energy function and (dashed grey line in Figure 3) eight CTP configurations selected. The energy was then minimized using steepest descent to the nearest local energy minimum and the resulting configuration used as input in a DFT/PBE calculation where again the energy was minimized. In all cases, the energy difference between the initial and final structure in the DFT calculations is around 5 eV (i.e. 0.03 eV per atom), mainly due to the fact that bond lengths are shorter for the potential functions used here as compared to the DFT/PBE values. Four of the systems retained the CTP configuration of the solvation shell, while the rest changed into the OH state. To account for the effect of finite temperature, the CTP configurations were heated up to 300 K using classical dynamics simulations and velocities initialised from a Maxwell distribution. During this heating procedure, the solvation shell reverted to the OH state before reaching 50 K. This is to be expected because of the high ion concentration and use of uniform background charge.

Despite the fact that the various potential energy functions all perform similarly well with respect to the hydration free energy and ion-oxygen distance, the relative stability and frequency of switching between the OH and CTP states vary significantly. For instance, the lifetime in the OH state, for a concentration of

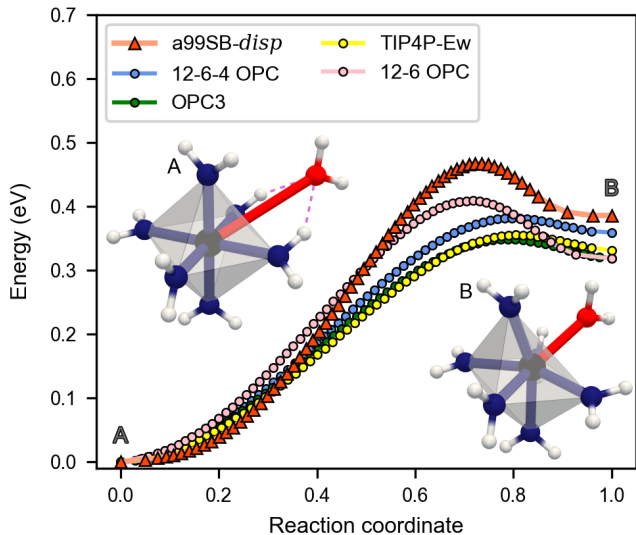


Figure 4: Energy profile along the minimum energy path obtained from CI-NEB calculations for the transition between the OH state (A) and the CTP state (B), using various potential energy functions: 12-6 potential with the a99SB-*disp* water model<sup>9</sup> and OPC models,<sup>9</sup> respectively, and the 12-6-4 potential with the OPC,<sup>8</sup> OPC3<sup>8</sup> and TIP4P-Ew<sup>12</sup> water models. An energy barrier exists between the local minima corresponding to the two states. Each system consists of a single  $\text{Fe}^{3+}$  ion and seven  $\text{H}_2\text{O}$  molecules. The central  $\text{Fe}^{3+}$  ion, H atoms, the six closest O atoms and the seventh O atom are coloured in black, light grey, blue and red, respectively. Hydrogen bonds formed by the seventh water molecule are depicted as pink dashed lines.

1:61, is 4.4 ns for the a99SB-*disp* water while it is 0.2 ns for the OPC parameterizations (see Table S2 in the Supplementary for more details).

Figure 4 depicts the energy barrier for the isolated ion-water clusters, determined using climbing image nudged-elastic band (CI-NEB)<sup>68–70</sup> calculations for the 12-6 potential with the a99SB-*disp* water model, and the 12-6-4 potential with the OPC, OPC3 and TIP4P-Ew models, respectively. The parametrization with the a99SB-*disp* water model has a higher and steeper energy barrier (of 0.46 eV), which may qualitatively explain why the OH state is relatively stable for this model. With the 12-6-4 parameterizations, the system ratchets between the OH and CTP states more rapidly.

**Table 1:** Comparison of various structural parameters for energy minimized configurations of isolated ion-water clusters containing seven water molecules, modelled using the  $\text{Fe}^{3+}$ - $\text{H}_2\text{O}$  parameterizations for the 12-6 potential with the a99SB-*disp*<sup>9</sup> and OPC<sup>9</sup> water models, respectively, and the 12-6-4 potential with the OPC,<sup>8</sup> OPC3<sup>8</sup> and TIP4P-Ew<sup>12</sup> water models, as well as using DFT calculations with the PBE and B3LYP functional approximations. The average of the distance (in Å) from the central ion to the six closest neighbours,  $\overline{r_{i \leq 6}}$ , and the distance of the ion from the seventh water molecule,  $r_7$ , are listed.

Model	OH config.		CTP config.	
	$\overline{r_{i \leq 6}}$	$r_7$	$\overline{r_{i \leq 6}}$	$r_7$
12-6 a99SB- <i>disp</i> <sup>9</sup>	2.026	3.606	2.091	2.162
12-6 OPC <sup>9</sup>	2.019	3.537	2.088	2.153
12-6-4 OPC <sup>8</sup>	2.020	3.508	2.091	2.208
12-6-4 OPC3 <sup>8</sup>	1.999	3.468	2.067	2.182
12-6-4 TIP4P-Ew <sup>12</sup>	1.980	3.454	2.049	2.174
DFT/PBE	2.055	3.620	2.121	2.253
DFT/B3LYP	2.055	3.767	2.124	2.278

We also note that the probability of observing the OH state, at any point in the trajectory, for the 12-6 and 12-6-4 parameterizations with the OPC, OPC3, TIP4P-Ew models, is egregiously low, less than 50% at the highest concentration (see Supplementary Table S2). This clearly deviates from expected behaviour. On the other hand, the 12-6 parameterization with the a99SB-*disp* water model always predicts the OH state as the dominant state, at all concentrations considered. The relative performance appears to be linked to inherent characteristics of the specific water model in the parameterization, as opposed to a quirk of the 12-6 or 12-6-4 potential parameterizations (both classes of potentials perform similarly for the OPC model; see Supplementary for more details).

All of these potential energy functions are parameterized to reproduce an experimental IOD value of  $2.031 \pm 0.019$  Å, along with the hydration free energy. In other words, they are intended to model an octahedral solvation shell with  $\overline{r_{i \leq 6}} \approx 2.03$  Å. Table 1 depicts structural parameters for minimized OH and CTP configurations, for all models considered in this work. The fact that a99SB-*disp* water performs significantly better than the other potential energy functions could be because the  $\overline{r_{i \leq 6}}$  value for the OH state in ion-water clusters is the closest to the experimental IOD value. Models that pro-

duce values of  $\overline{r_{i \leq 6}}$  that are closer to the desired IOD value in the CTP state (for instance, the parameterization with TIP4P-Ew<sup>12</sup>) overemphasize the CTP state. Further investigation is needed to gain better understanding of the features that dictate how well these rigid fixed point-charge/water models can reproduce the true interaction between the ion and the water molecules.

Additionally, a geometry optimization of an isolated  $[\text{Fe}(\text{H}_2\text{O})_7]^{3+}$  cluster was performed using DFT with the PBE and B3LYP functionals, starting with the CTP minimal energy configuration obtained with the a99SB-*disp* potential energy function. The CTP configuration of the water molecules could be maintained during careful energy minimization, but the energy barrier for a transformation to the OH state turns out to be low (see Table 1 and Supporting). Therefore, the DFT results indicate that a CTP configuration is possible but is more likely as a metastable state in ‘bulk’ solution.

In conclusion, we find that the higher coordination numbers reported from simulations using empirical potential energy functions arise from the formation of a metastable solvation shell with 7 water molecules in a CTP geometry, in addition to the usual octahedral solvation shell. Our results indicate that the CTP state should be rare at high ion concentration,

and that many potential energy functions tend to overestimate its existence. Parameterization with the a99SB-*disp* water model is the most performant of the empirical potential energy functions tested, producing stable and long-lived OH states (see Supplementary Section 2 for a detailed comparison). The simulations reveal a strong dependence of the relative probability of the two states on the ion concentration. Also, the use of a uniform background charge, instead of explicit counterions tends to spuriously favour the OH state at high ion concentration. It is possible that DFT calculations have not exhibited the CTP state, as they may have been started from initial configurations with OH geometry, and have necessarily been carried out for short timescale, high ion concentration, using uniform background charge rather than explicit counterions. Our DFT results indicate that the hepta-coordinate CTP configurations can indeed be metastable in bulk solution. Further investigation, via experiments and electronic structure calculations for low ion concentrations and explicit counterions, is warranted to affirm the existence of the predicted CTP state.

## Methods

Classical dynamics simulations are carried out for a range in ion concentrations using potential energy functions and the LAMMPS software.<sup>71</sup> The simulated system consists of  $\text{Fe}^{3+}$ ,  $\text{Cl}^-$  ions and  $\text{H}_2\text{O}$  molecules modeled by fixed-charge rigid water models, in such a way as to maintain charge neutrality. For comparison, simulations are also carried out using uniform negative background instead of explicit  $\text{Cl}^-$  ions since this is often done in DFT calculations. We show that averages of structural properties are equivalent for systems with the same ionic concentration, irrespective of the simulation box size (Supplementary Section 1).

The  $\text{Fe-H}_2\text{O}$  non-bonded interactions consist of Coulombic electrostatic contributions and 12-6 Lennard-Jones (LJ) potential,<sup>72</sup> or by the 12-6-4 Lennard-Jones potential.<sup>13</sup> These functional forms have been specifically parameter-

ized for use with each  $\text{H}_2\text{O}$  model and for the  $\text{Fe}^{3+}$  ion. We have used the  $\text{Fe-H}_2\text{O}$  parameterizations from Zhang et al.<sup>9</sup> and Li et al.<sup>8,12</sup> for the 12-6 potential with the a99SB-*disp*  $\text{H}_2\text{O}$ <sup>73</sup> model, the 12-6-4 potential with OPC<sup>74</sup> and OPC3<sup>75</sup>  $\text{H}_2\text{O}$  models, and the 12-6-4 potential with the TIP4P-Ew<sup>76</sup>  $\text{H}_2\text{O}$  model, respectively. Parameters for chloride-chloride interactions were obtained from Smith and Dang<sup>77</sup>, which have previously been used in a study of  $\text{FeCl}_2$  in water.<sup>78</sup> Cross-interactions involving LJ interactions were calculated using the Lorentz-Berthelot mixing rules. Unless otherwise mentioned, all the simulations make use the a99SB-*disp* parameterization.

About 4000  $\text{H}_2\text{O}$  molecules were used and the ionic concentration varied by creating initial simulation configurations with different number of ions placed randomly via PACKMOL.<sup>79</sup> Energy minimization was first performed using 1000 steps of steepest descent and 1000 subsequent steps of conjugate gradient, with a timestep of 0.001 fs. Equilibration at 300 K was attained by performing simulations in the NPT ensemble, for at least 25 ns. This was followed by another equilibration run in the NVT ensemble, at 300 K, for 5.5 ns. The production simulations were conducted in the NVT ensemble for long time intervals, ranging from 50-150 ns. The time step used was 1 fs, and the temperature and pressure were controlled by the Nosé-Hoover thermostat and barostat.<sup>80</sup> The long-range electrostatics were treated with the particle-particle particle-mesh (PPPM) algorithm.<sup>81</sup> The shape of the water molecules was constrained by the SHAKE algorithm.<sup>82</sup>

The DFT calculations were carried out using the Perdew-Burke-Ernzerhof (PBE)<sup>83</sup> exchange correlation functional and a plane wave basis set as implemented in the VASP software<sup>84,85</sup> and using the B3LYP functional<sup>86,87</sup> and the def2-TZVP basis set<sup>88</sup> as implemented in the ORCA software.<sup>89,90</sup> The system used in the DFT/PBE calculations consisted of 64 water molecules and an  $\text{Fe}^{+3}$  ion in a cubic simulation cell of length 12.44 Å with periodic boundary conditions. The fixed volume simulation box was obtained from quenching the ion-water system with the a99SB-*disp* param-

eterization, corresponding to the ‘density’ of a 64 times larger simulation box equilibrated in the NPT ensemble with the same ionic concentration (1.64%). The plane-wave energy cutoff was set to 500 eV and a  $\Gamma$ -point only sampling of the first Brillouin zone was used. The energy minimization of atomic configurations was carried out until the magnitude of atomic forces had dropped below 0.02 eV/Å.

Snapshots and visuals of solvation systems were created using `solvis` (<https://github.com/amritagos/solvis>). Scripts for calculating the sphericity of solvation shells are also provided in the same.

**Acknowledgement** This work was funded by the Icelandic Research Fund (grants 228615-051 and 207283-053). The calculations were performed using compute resources provided by the Icelandic Research Electronic Infrastructure (IREI). A.G. is grateful to Moritz Sallermann and Rohit Goswami for fruitful discussions.

## Supporting Information Available

The authors confirm that the data supporting the findings of this study are available within the article and/or its supplementary materials. The supporting information contains data on the validation of ion concentration effects as well as finite size effects; comparison of results using various potential energy functions.

## References

- (1) Ohtaki, H.; Radnai, T. Structure and dynamics of hydrated ions. *Chem. Rev.* **1993**, *93*, 1157–1204.
- (2) Amira, S.; Spångberg, D.; Probst, M.; Hermansson, K. Molecular Dynamics Simulation of  $\text{Fe}^{2+}(\text{aq})$  and  $\text{Fe}^{3+}(\text{aq})$ . *The Journal of Physical Chemistry B* **2004**, *108*, 496–502.
- (3) Qing, Y.; Xing, C.; Jing, Z.; Hai-Feng, Z.; Wang-Sheng, C.; Xu-Sheng, Z.; Zi-Yu, W. Local hydrated structure of an  $\text{Fe}^{2+}/\text{Fe}^{3+}$  aqueous solution: an investigation using a combination of molecular dynamics and X-ray absorption fine structure methods. *Chinese Physics C* **2013**, *37*, 038003–038003.
- (4) Li, P.; Roberts, B. P.; Chakravorty, D. K.; Merz, K. M. Rational Design of Particle Mesh Ewald Compatible Lennard-Jones Parameters for +2 Metal Cations in Explicit Solvent. *J. Chem. Theory Comput.* **2013**, *9*, 2733–2748.
- (5) Chillemi, G.; D’Angelo, P.; Pavel, N. V.; Sanna, N.; Barone, V. Development and Validation of an Integrated Computational Approach for the Study of Ionic Species in Solution by Means of Effective Two-Body Potentials. The Case of  $\text{Zn}^{2+}$ ,  $\text{Ni}^{2+}$ , and  $\text{Co}^{2+}$  in Aqueous Solutions. *J. Am. Chem. Soc.* **2002**, *124*, 1968–1976.
- (6) Joung, I. S.; Cheatham, T. E. Molecular Dynamics Simulations of the Dynamic and Energetic Properties of Alkali and Halide Ions Using Water-Model-Specific Ion Parameters. *J. Phys. Chem. B* **2009**, *113*, 13279–13290.
- (7) Duarte, F.; Bauer, P.; Barrozo, A.; Amrein, B. A.; Purg, M.; Åqvist, J.; Kamerlin, S. C. L. Force Field Independent Metal Parameters Using a Nonbonded Dummy Model. *J. Phys. Chem. B* **2014**, *118*, 4351–4362.
- (8) Li, Z.; Song, L. F.; Li, P.; Merz, K. M. Parametrization of Trivalent and Tetravalent Metal Ions for the OPC3, OPC, TIP3P-FB, and TIP4P-FB Water Models. *J. Chem. Theory Comput.* **2021**, *17*, 2342–2354.
- (9) Zhang, Y.; Jiang, Y.; Qiu, Y.; Zhang, H. Rational Design of Nonbonded Point Charge Models for Highly Charged Metal Cations with Lennard-Jones 12-6 Potential. *J. Chem. Inf. Model.* **2021**, *61*, 4613–4629.

- (10) Li, Z.; Song, L. F.; Li, P.; Merz, K. M. Systematic Parametrization of Divalent Metal Ions for the OPC3, OPC, TIP3P-FB, and TIP4P-FB Water Models. *J. Chem. Theory Comput.* **2020**, *16*, 4429–4442.
- (11) Zhang, Y.; Jiang, Y.; Peng, J.; Zhang, H. Rational Design of Nonbonded Point Charge Models for Divalent Metal Cations with Lennard-Jones 12-6 Potential. *J. Chem. Inf. Model.* **2021**, *61*, 4031–4044.
- (12) Li, P.; Song, L. F.; Merz, K. M. Parameterization of Highly Charged Metal Ions Using the 12-6-4 LJ-Type Nonbonded Model in Explicit Water. *The Journal of Physical Chemistry B* **2014**, *119*, 883–895.
- (13) Li, P.; Merz, K. M. Taking into Account the Ion-Induced Dipole Interaction in the Nonbonded Model of Ions. *J. Chem. Theory Comput.* **2013**, *10*, 289–297.
- (14) Lewis, D. L.; Lippard, S. J. Structure of heptakis(tert-butyl isocyanide)molybdenum(II) hexafluorophosphate, a seven-coordinate complex with C<sub>2</sub>h symmetry. *J. Am. Chem. Soc.* **1975**, *97*, 2697–2702.
- (15) Yi, G.; Cui, H.; Zhang, C.; Zhao, W.; Chen, L.; Zhang, Y.-Q.; Chen, X.-T.; Song, Y.; Yuan, A. A capped trigonal prismatic cobalt(II) complex as a structural archetype for single-ion magnets. *Dalton Trans.* **2020**, *49*, 2063–2067.
- (16) Haiges, R.; Boatz, J.; Yousufuddin, M.; Christe, K. Monocapped Trigonal-Prismatic Transition-Metal Heptaazides: Syntheses, Properties, and Structures of [Nb(N<sub>3</sub>)<sub>7</sub>]<sup>2-</sup> and [Ta(N<sub>3</sub>)<sub>7</sub>]<sup>2-</sup>. *Angew. Chem. - Int. Ed.* **2007**, *46*, 2869–2874.
- (17) Lin, Z.; Bytheway, I. Stereochemistry of Seven-Coordinate Main Group and d<sub>0</sub> Transition Metal Molecules. *Inorg. Chem.* **1996**, *35*, 594–603.
- (18) Huang, L.; Peng, Y.; Li, Z.; Wei, Z.; Hughes, D. L.; Zeng, X.; Luo, Q.; Liu, X. Two Hg(II) complexes with a capped trigonal prismatic geometry derived from multidentate macrocyclic ligands containing N and S donors, with coordinated anions. *Inorg. Chim. Acta* **2010**, *363*, 2664–2667.
- (19) Chillemi, G.; Mancini, G.; Sanna, N.; Barone, V.; Longa, S. D.; Benfatto, M.; Pavel, N. V.; D'Angelo, P. Evidence for Sevenfold Coordination in the First Solvation Shell of Hg(II) Aqua Ion. *J. Am. Chem. Soc.* **2007**, *129*, 5430–5436.
- (20) Richens, D. T. *The Chemistry of Aqua ions: Synthesis, Structure, and Reactivity: a Tour through the Periodic Table of the Elements*; Wiley New York, 1997.
- (21) Li, P. Bridging the 12-6-4 Model and the Fluctuating Charge Model. *Frontiers in Chemistry* **2021**, *9*, 721960.
- (22) Aqvist, J.; Warshel, A. Free energy relationships in metalloenzyme-catalyzed reactions. Calculations of the effects of metal ion substitutions in staphylococcal nuclease. *J. Am. Chem. Soc.* **1990**, *112*, 2860–2868.
- (23) Liao, Q.; Pabis, A.; Strodel, B.; Kamerlin, S. C. L. Extending the Nonbonded Cationic Dummy Model to Account for Ion-Induced Dipole Interactions. *J. Phys. Chem. Lett* **2017**, *8*, 5408–5414.
- (24) Magini, M.; Radnai, T. X-ray diffraction study of ferric chloride solutions and hydrated melt. Analysis of the iron (III)–chloride complexes formation. *J. Chem. Phys.* **1979**, *71*, 4255–4262.
- (25) Magini, M. Solute structuring in iron (III) chloride solutions. II. Evidence of polynuclear complex formation in the FeCl<sub>3</sub>·6H<sub>2</sub>O melt by the “isoelectronic solutions” method. *The Journal of Chemical Physics* **1982**, *76*, 1111–1115.
- (26) Giubileo, G.; Magini, M.; Licheri, G.; Paschina, G.; Piccaluga, G.; Pinna, G.

- On the structure of iron(III) chloride solutions. *Inorg. Chem.* **1983**, *22*, 1001–1002.
- (27) Gammons, C. H.; Allin, N. C. Stability of aqueous Fe(III) chloride complexes and the solubility of hematite between 150 and 300°C. *Geochim. Cosmochim. Acta* **2022**, *330*, 148–164.
- (28) Brady, G. W.; Robin, M. B.; Varimbi, J. The Structure of Ferric Chloride in Neutral and Acid Solutions. *Inorg. Chem.* **1964**, *3*, 1168–1173.
- (29) Lind, M. D. Structure of Ferric Chloride in Aqueous Solutions. *J. Chem. Phys.* **1967**, *46*, 2010–2011.
- (30) Wertz, D. L.; Steele, M. L. Coordination of iron(3+) ion in concentrated aqueous solutions with chloride ligands. *Inorg. Chem.* **1980**, *19*, 1652–1656.
- (31) Wertz, D. L.; Luter, M. D. Evolving cation coordination in aqueous solutions prepared from iron(III) chloride hexahydrate. *Inorg. Chem.* **1981**, *20*, 3118–3119.
- (32) Luter, M. D.; Wertz, D. L. Existence of tetrachloroironate(III) in hydrochloric acid solutions. *J Phys. Chem.* **1981**, *85*, 3542–3543.
- (33) Brady, G. W. Structure in Ionic Solutions. III. *J. Chem. Phys.* **1958**, *29*, 1371–1375.
- (34) Standley, C. L.; Kruh, R. F. On the Structure of Ferric Chloride Solutions. *J. Chem. Phys.* **1961**, *34*, 1450–1451.
- (35) Persson, I. Ferric Chloride Complexes in Aqueous Solution: An EXAFS Study. *J. Solution Chem.* **2018**, *47*, 797–805.
- (36) Smirnov, P. R.; Grechin, O. V. Structure of the nearest surrounding of ions in aqueous solutions of iron(III) chloride by X-ray diffraction method. *J. Mol. Liq.* **2019**, *281*, 385–388.
- (37) Baumler, S. M.; V., W. H. H.; Allen, H. C. Hydration of ferric chloride and nitrate in aqueous solutions: water-mediated ion pairing revealed by Raman spectroscopy. *Phys. Chem. Chem. Phys.* **2019**, *21*, 19172–19180.
- (38) Munoz-Paez, A.; Diaz, S.; Perez, P.; Martín-Zamora, M.; Martinez, J.; Pappalardo, R.; Marcos, E. S. EXAFS investigation of the second hydration shell of metal cations in dilute aqueous solutions. *Physica B: Condensed Matter* **1995**, *208*, 395–397.
- (39) Thompson, A. C.; Vaughan, D., et al. *X-ray data booklet*; Lawrence Berkeley National Laboratory, University of California Berkeley, CA, 2001; Vol. 8.
- (40) Sit, P.-L.; Cococcioni, M.; Marzari, N. Realistic quantitative descriptions of electron transfer reactions: Diabatic free-energy surfaces from first-principles molecular dynamics. *Physical Review Letters* **2006**, *97*, 028303.
- (41) Bogatko, S. A.; Bylaska, E. J.; Weare, J. H. First Principles Simulation of the Bonding, Vibrational, and Electronic Properties of the Hydration Shells of the High-Spin Fe<sup>3+</sup> Ion in Aqueous Solutions. *The Journal of Physical Chemistry A* **2010**, *114*, 2189–2200.
- (42) Lei, X. L.; Pan, B. C. The Structural Features of the Hydrated Ferrous Ion Clusters: [Fe(H<sub>2</sub>O)<sub>n</sub>]<sup>2+</sup> (n = 1–19). *Journal of Cluster Science* **2012**, *23*, 311–324.
- (43) Nazmutdinov, R. R.; Zinkicheva, T. T.; Kolpakov, M. E.; Dresvyannikov, A. F. Quantum Chemical Modeling of Electrochemical Consecutive Reduction of Fe(III) Aqua- and Aqua-Hydroxocomplexes. *Journal of Structural Chemistry* **2019**, *60*, 1226–1233.
- (44) Mandal, S.; Kar, R.; Meyer, B.; Nair, N. N. Hybrid Functional and Plane Waves based Ab Initio Molecular Dynamics Study of the Aqueous Fe<sup>2+</sup>/Fe<sup>3+</sup> Redox Reaction. *ChemPhysChem* **2023**, *24*, e202200617.

- (45) Wadell, H. Volume, Shape, and Roundness of Quartz Particles. *The Journal of Geology* **1935**, *43*, 250–280.
- (46) Sau, T. K.; Pal, A.; Jana, N.; Wang, Z.; Pal, T. *J. Nanoparticle Res. Interdiscip. Forum Nanoscale Sci. Technol.* **2001**, *3*, 257–261.
- (47) Stevenson, A. P.; Bea, D. B.; Civit, S.; Contera, S. A.; Cerveto, A. I.; Trigueros, S. Three strategies to stabilise nearly monodispersed silver nanoparticles in aqueous solution. *Nanoscale Res. Lett.* **2012**, *7*.
- (48) Mo, X.; Xiang, H.; Wei, L.; Xia, L.; Chen, X.; Chen, Y.; Zhang, B. Nature-inspired allomelanin nanomedicine alleviates cardiac ischemia/reperfusion injury via scavenging free radicals and ameliorating myocardial microenvironment. *Nano Today* **2022**, *46*, 101589.
- (49) You, X. Nanoparticle Sphericity Investigation of Cu-Al<sub>2</sub>O<sub>3</sub>-H<sub>2</sub>O Hybrid Nanofluid Flows between Inclined Channels Filled with a Porous Medium. *Nanomaterials* **2022**, *12*, 2552.
- (50) Nimmagadda, R.; Venkatasubbaiah, K. Numerical Investigation on Conjugate Heat Transfer Performance of Microchannel Using Sphericity-Based Gold and Carbon Nanoparticles. *Heat Transfer Eng.* **2016**, *38*, 87–102.
- (51) Hakim, L. F.; Portman, J. L.; Casper, M. D.; Weimer, A. W. Aggregation behavior of nanoparticles in fluidized beds. *Powder Technol.* **2005**, *160*, 149–160.
- (52) Szebeni, J.; Bedőcs, P.; Rozsnyay, Z.; Weiszár, Z.; Urbanics, R.; Rosivall, L.; Cohen, R.; Garbuzenko, O.; Báthori, G.; Tóth, M. et al. Liposome-induced complement activation and related cardiopulmonary distress in pigs: factors promoting reactogenicity of Doxil and AmBisome. *Nanomedicine: Nanotechnology, Biology and Medicine* **2012**, *8*, 176–184.
- (53) Stater, E. P.; Sonay, A. Y.; Hart, C.; Grimm, J. The ancillary effects of nanoparticles and their implications for nanomedicine. *Nat. Nanotechnology* **2021**, *16*, 1180–1194.
- (54) Li, W.; Newitt, D. C.; Yun, B. L.; Jones, E. F.; Arasu, V.; Wilmes, L. J.; Gibbs, J.; Nguyen, A. A.-T.; Onishi, N.; Kornak, J. et al. Tumor Sphericity Predicts Response in Neoadjuvant Chemotherapy for Invasive Breast Cancer. *Tomography* **2020**, *6*, 216–222.
- (55) Davey, A.; van Herk, M.; Faivre-Finn, C.; Mistry, H.; McWilliam, A. Is tumour sphericity an important prognostic factor in patients with lung cancer? *Radiother Oncol* **2020**, *143*, 73–80.
- (56) Szeto, M. D.; Chakraborty, G.; Hadley, J.; Rockne, R.; Muzi, M.; Alvord, E. C.; Krohn, K. A.; Spence, A. M.; Swanson, K. R. Quantitative Metrics of Net Proliferation and Invasion Link Biological Aggressiveness Assessed by MRI with Hypoxia Assessed by FMISO-PET in Newly Diagnosed Glioblastomas. *Cancer Res.* **2009**, *69*, 4502–4509.
- (57) Kingston, B. R.; Syed, A. M.; Ngai, J.; Sindhwani, S.; Chan, W. C. W. Assessing micrometastases as a target for nanoparticles using 3D microscopy and machine learning. *Proc. Natl. Acad. Sci.* **2019**, *116*, 14937–14946.
- (58) Shin, J.; Lim, J. S.; Huh, Y.-M.; Kim, J.-H.; Hyung, W. J.; Chung, J.-J.; Han, K.; Kim, S. A radiomics-based model for predicting prognosis of locally advanced gastric cancer in the preoperative setting. *Sci. Rep.* **2021**, *11*, 1879.
- (59) Baysal, I.; Ucar, G.; Gultekinoglu, M.; Ulubayram, K.; Yabanoglu-Ciftci, S. Donepezil loaded PLGA-b-PEG nanoparticles: their ability to induce destabilization of amyloid fibrils and to cross blood brain barrier in vitro. *J Neural Transm* **2016**, *124*, 33–45.

- (60) Li, T.; Li, S.; Zhao, J.; Lu, P.; Meng, L. Sphericities of non-spherical objects. *Particurology* **2012**, *10*, 97–104.
- (61) Bullard, J. W.; Garboczi, E. J. Defining shape measures for 3D star-shaped particles: Sphericity, roundness, and dimensions. *Powder Technol.* **2013**, *249*, 241–252.
- (62) Zheng, K.; Du, C.; Li, J.; Qiu, B.; Fu, L.; Dong, J. Numerical simulation of the impact-breakage behavior of non-spherical agglomerates. *Powder Technol.* **2015**, *286*, 582–591.
- (63) Ester, M.; Kriegel, H.-P.; Sander, J.; Xu, X. A Density-Based Algorithm for Discovering Clusters in Large Spatial Databases with Noise. Proceedings of the Second International Conference on Knowledge Discovery and Data Mining. 1996; p 226–231.
- (64) Schubert, E.; Sander, J.; Ester, M.; Kriegel, H. P.; Xu, X. DBSCAN Revisited, Revisited. *ACM Transactions on Database Systems* **2017**, *42*, 1–21.
- (65) Pedregosa, F.; Varoquaux, G.; Gramfort, A.; Michel, V.; Thirion, B.; Grisel, O.; Blondel, M.; Prettenhofer, P.; Weiss, R.; Dubourg, V. et al. Scikit-learn: Machine Learning in Python. *J Mach Learn Res* **2011**, *12*, 2825–2830.
- (66) Hoffmann, R.; Beier, B. F.; Muetterties, E. L.; Rossi, A. R. Seven-coordination. A molecular orbital exploration of structure, stereochemistry, and reaction dynamics. *Inorg. Chem.* **1977**, *16*, 511–522.
- (67) Casanova, D.; Alemany, P.; Bofill, J. M.; Alvarez, S. Shape and Symmetry of Heptacoordinate Transition-Metal Complexes: Structural Trends. *Chemistry – A European Journal* **2003**, *9*, 1281–1295.
- (68) Henkelman, G.; Jónsson, H. Improved tangent estimate in the nudged elastic band method for finding minimum energy paths and saddle points. *J. Chem. Phys.* **2000**, *113*, 9978–9985.
- (69) Henkelman, G.; Uberuaga, B. P.; Jónsson, H. A climbing image nudged elastic band method for finding saddle points and minimum energy paths. *J. Chem. Phys.* **2000**, *113*, 9901–9904.
- (70) Ásgeirsson, V.; Jónsson, H. In *Handbook of Materials Modeling: Methods: Theory and Modeling*; Andreoni, W., Yip, S., Eds.; Springer International Publishing: Cham, 2020; pp 689–714.
- (71) Thompson, A. P.; Aktulga, H. M.; Berger, R.; Bolintineanu, D. S.; Brown, W. M.; Crozier, P. S.; in 't Veld, P. J.; Kohlmeyer, A.; Moore, S. G.; Nguyen, T. D. et al. LAMMPS - a flexible simulation tool for particle-based materials modeling at the atomic, meso, and continuum scales. *Comput. Phys. Commun.* **2022**, *271*, 108171.
- (72) Lennard-Jones, J. E. Cohesion. *Proc. Phys. Soc.* **1931**, *43*, 461–482.
- (73) Robustelli, P.; Piana, S.; Shaw, D. E. Developing a molecular dynamics force field for both folded and disordered protein states. *Proc. Natl. Acad. Sci.* **2018**, *115*.
- (74) Izadi, S.; Anandakrishnan, R.; Onufriev, A. V. Building Water Models: A Different Approach. *J. Phys. Chem. Lett* **2014**, *5*, 3863–3871.
- (75) Izadi, S.; Onufriev, A. V. Accuracy limit of rigid 3-point water models. *J. Chem. Phys.* **2016**, *145*.
- (76) Horn, H. W.; Swope, W. C.; Pitner, J. W.; Madura, J. D.; Dick, T. J.; Hura, G. L.; Head-Gordon, T. Development of an improved four-site water model for biomolecular simulations: TIP4P-Ew. *J. Chem. Phys.* **2004**, *120*, 9665–9678.
- (77) Smith, D. E.; Dang, L. X. Computer simulations of NaCl association in polarizable

- water. *J. Chem. Phys.* **1994**, *100*, 3757–3766.
- (78) Lümme, N.; Kvamme, B. Properties of aging FeCl<sub>2</sub> clusters grown in supercritical water investigated by molecular dynamics simulations. *J. Chem. Phys.* **2010**, *132*.
- (79) Martínez, L.; Andrade, R.; Birgin, E. G.; Martínez, J. M. PACKMOL: A package for building initial configurations for molecular dynamics simulations. *J. Comput. Chem.* **2009**, *30*, 2157–2164.
- (80) Shinoda, W.; Shiga, M.; Mikami, M. Rapid estimation of elastic constants by molecular dynamics simulation under constant stress. *Phys. Rev. B* **2004**, *69*, 134103.
- (81) Hockney, R. W.; Eastwood, J. W. *Computer simulation using particles*; crc Press, 2021.
- (82) Ryckaert, J.-P.; Ciccotti, G.; Berendsen, H. J. Numerical integration of the cartesian equations of motion of a system with constraints: molecular dynamics of n-alkanes. *J. Comput. Phys.* **1977**, *23*, 327–341.
- (83) Perdew, J. P.; Burke, K.; Ernzerhof, M. Generalized Gradient Approximation Made Simple. *Phys. Rev. Lett.* **1996**, *77*, 3865–3868.
- (84) Kresse, G.; Furthmüller, J. Efficient iterative schemes for ab initio total-energy calculations using a plane-wave basis set. *Phys. Rev. B* **1996**, *54*, 11169–11186.
- (85) Kresse, G.; Joubert, D. From ultrasoft pseudopotentials to the projector augmented-wave method. *Phys. Rev. B* **1999**, *59*, 1758–1775.
- (86) Becke, A. D. Density-functional exchange-energy approximation with correct asymptotic behavior. *Phys. Rev. A* **1988**, *38*, 3098–3100.
- (87) Becke, A. D. Density-functional thermochemistry. III. The role of exact exchange. *J. Chem. Phys.* **1993**, *98*, 5648–5652.
- (88) Weigend, F.; Ahlrichs, R. Balanced basis sets of split valence, triple zeta valence and quadruple zeta valence quality for H to Rn: Design and assessment of accuracy. *Phys. Chem. Chem. Phys.* **2005**, *7*, 3297–3305.
- (89) Neese, F. The ORCA program system. *Wiley Interdiscip. Rev. Comput. Mol. Sci.* **2012**, *2*, 73–78.
- (90) Neese, F. Software update: The ORCA program system—Version 5.0. 2022.